Available online at www.sciencedirect.com
SCIENCE DIRECT®
PERGAMON
International Journal of Heat and Mass Transfer 46 (2003) 1293–1307
International Journal of HEAT and MASS TRANSFER
www.elsevier.com/locate/ijhmt

Pore network simulations of drying of capillary porous media. Influence of thermal gradients

F. Plourde [a], M. Prat [b,*]

[a] LET/ENSMA 1, Avenue Clément Ader, Teleport 2, BP 40109, 86961 Futuroscope Cedex, France
[b] Institut de Mécanique des Fluides de Toulouse, UMR CNRS-INP/UPS No. 5502, Avenue du Professeur Camille Soula, 31400 Toulouse, France

Received 20 November 2000; received in revised form 4 December 2001

Abstract

A pore network model of drying with heat transfer is developed. The model is applied to study the influence of surface tension gradients induced by thermal gradients on the phase distribution within a capillary porous medium. The numerical simulations show that surface tension gradients can lead to invasion percolation in a destabilizing gradient (IPDG) patterns or invasion percolation in a stabilizing gradient patterns depending on the sign of thermal gradient. The surface tension gradient effect is shown to be significant for sufficiently weakly disordered porous media. The results are summarized on a phase diagram delineating the various patterns that can be expected as functions of thermal gradient and disorder parameter. This diagram is pertinent to situations where occupation probability gradients induced by viscous or gravity effects are negligible.

The results also indicate the possibility of a somewhat paradoxical convective drying situation when thermal gradients and disorder are such that a IPDG pattern develops. In this case, contrary to more conventional situations, it may be much more efficient to blow an air colder than the porous medium initial temperature.

1. Introduction

Drying of capillary porous media has been the subject of many studies (see for instance [1] and references therein) and is still a challenging modelling problem. This is not surprising if one considers that drying involves complex transport processes, such as two-phase flow with liquid–vapor phase change in porous media, and that numerous aspects of drying are of interest from a practical standpoint. For some materials, such as wood for instance, the mechanical aspects (deformation, shrinkage, fracturing) are of a great importance. For foodstuffs, constraints linked to the final quality of the product must be taken into account. For all products, however, the most basic aspect of drying is the drying kinetics, which in turn depends on the evolution of the water distribution within the materials during drying. Hence, one of the most basic aspects of drying is the understanding of the phase distribution evolution and the identification of the key-factors affecting this evolution. Recently, it has been shown that insights into this aspect could be gained from pore network models (see [2–4] and references therein). In those works, influence of thermal gradients was ignored. Energy aspects are, however, of uttermost importance in drying and drying situations where thermal effects are negligible are clearly an exception. The objective of the present work is therefore to shed light on the influence of the thermal gradients that usually develop during drying. As in the previous studies based on pore network models of drying, we investigate situations under relatively slow drying conditions, i.e. temperatures well below the boiling temperature, so that development of total pressure gradients in the gas phase can be ignored. To this end, a

* Corresponding author. Tel.: +33-561-28-58-83; fax: +33-561-28-59-93.
E-mail addresses: plourde@let.ensma.fr (F. Plourde), prat@imft.fr (M. Prat).

0017-9310/03/$ - see front matter © 2002 Elsevier Science Ltd. All rights reserved.
PII: S0017-9310(02)00391-5

Nomenclature

a	lattice spacing (m)
$Ca = \mu v/\gamma$	capillary number
$B = \Delta\rho g a^2/\gamma$	bond number
D	binary diffusion coefficient (m^2/s)
e	pore network thickness (m)
h	mass transfer coefficient at the interface
K	permeability (m^2)
ℓ	bond width (m)
ℓ_{min}	minimum bond width (m)
ℓ_{max}	maximum bond width (m)
L	sample size (m)
L_g	characteristic length associated with gravity effect (m)
L_{cap}	characteristic length associated with viscous effects (m)
L_T	characteristic length associated with thermal gradient (m)
M_v	vapor molecular weight (kg/kmol)
p	occupation probability
P	gas phase total pressure (Pa)
P_c	capillary pressure (Pa)
P_{cth}	threshold capillary pressure (Pa)
P_v	vapor partial pressure (Pa)
P_{sat}	saturation vapor partial pressure (Pa)
$P_{v\infty}$	vapor partial pressure in the incident air (Pa)
r	meniscus curvature radius (m)
R	universal gas constant (J/kmol/K)
T	temperature (°C)
v	liquid characteristic velocity (m/s)
z	spatial coordinate (m)
ε	porosity of porous medium
Δh_{vap}	enthalpy of vaporisation (J/kg)
γ	surface tension (N/m)
μ	liquid dynamic viscosity (Pl)
λ	thermal conductivity (W/m/°C)
λ_s	solid phase thermal conductivity (W/m/°C)
λ_l	liquid phase thermal conductivity (W/m/°C)
λ_v	gas phase thermal conductivity (W/m/°C)
λ_l^*	effective thermal conductivity of porous medium saturated by the liquid phase (W/m/°C)
λ_v^*	effective thermal conductivity of porous medium saturated by the gas phase (W/m/°C)
ρ	liquid phase density (kg/m^3)
Σ	disorder parameter (m)

pore network model of drying including the computation of the temperature field has been developed. As in the pore network studies mentioned before, invasion percolation (IP) in a gradient (see [5] and references therein) will be the appropriate theoretical framework for analysing the results. As discussed in previous works (e.g. [2,5]) the phase distribution under slow drying conditions and in the absence of thermal gradient is controlled by the interplay of capillary, viscous and gravity forces. In the absence of significant gravity or viscous effects, IP patterns are expected. As discussed in [5], viscous effects are always stabilizing in slow drying and therefore lead to patterns characteristic of invasion in a stabilizing gradient (IPSG patterns). As shown in [6], gravity effects can be destabilizing, i.e. leading to patterns characteristic of invasion in a destabilizing gradient (IPDG), or stabilizing, i.e. leading to invasion percolation in a stabilizing gradient (IPSG) patterns, depending on the orientation of gravity vector with respect to the main direction of invasion. These various patterns are summarised on the phase diagram shown in Fig. 1. In this figure, Ca is the capillary number, which is the ratio between viscous and capillary forces. B is the bond number, ratio between gravity and capillary forces. Ca is defined as $Ca = \mu v/\gamma$ where v is a characteristic liquid filtration velocity, μ the liquid dynamic viscosity and γ the surface tension. B is defined as $B = \rho_l g a^2/\gamma$ where a is the lattice spacing, g the acceleration of gravity and ρ_l the liquid density. As explained in [5] or [6], the diagram shown in Fig. 1 is obtained by comparing three length scales, the sample length L, the length L_g which characterizes the typical size of a front stabilized by gravity and the length L_{cap} which characterizes the typical size of a front stabilized by viscous effects. For two-dimensional (2D) systems, L_g and L_{cap} scale as [5]

$$L_g \propto \left(\frac{B}{\Sigma^*}\right)^{-0.52}; \quad L_{cap} \propto \left(\frac{Ca}{\Sigma^*}\right)^{-0.52} \tag{1}$$

where Σ^* is a parameter that characterizes the disorder of the porous medium, i.e. the width of the pore size distribution ($\Sigma^* = (\ell_{max}/a) - (\ell_{min}/a)$ where a is the lattice spacing, ℓ_{min} the width of the narrowest bond and ℓ_{max} the width of the widest bond of the pore network). As can be seen from Fig. 1, significant gravity or viscous effects dramatically affect the invasion pattern and thereby the drying rates. In this paper, we concentrate on the IP domain (capillary fingering domain) and explore the various invasion patterns that can be obtained in the absence of significant gravity or viscous effects, when thermal gradients are present. For simplicity, the simulations have been performed in 2D. However, the main results obtained can be qualitatively extended to three-dimensional (3D) systems.

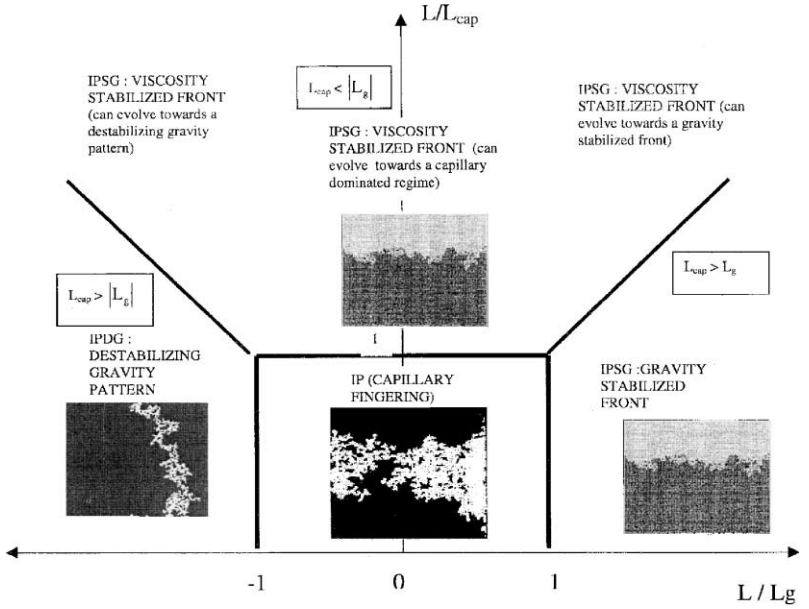

Fig. 1. Drying phase diagram in the absence of thermal gradient effects. L is the sample size. L_{cap} is the length over which the pressure drop due to viscous effects is of the order of the capillary pressure. L_g is the length over which the pressure variation due to gravity effects is of the order of the capillary pressure.

Before going into the details of the present study, it is worth recalling that the influence of thermal gradients on the moisture migration in non-saturated porous media or during the drying of capillary porous media has been the subject of numerous studies in the fundamentally different context of the continuum approach to porous media. Here, we briefly review some of these studies, restricting ourselves to drying with temperatures well below the boiling point. Philip and de Vries [7] were the first to establish theoretically that thermal gradients could induce a moisture transport in liquid phase and in gas phase. The mass flux in gas phase due to thermal gradients was shown to be induced by the dependence of the saturation vapor partial pressure on temperature whereas the mass flux in liquid phase was shown to be a consequence of the dependence of the capillary pressure on temperature via the surface tension. Naturally, these two effects are present in the pore network simulations presented in this paper. In the present study, however, we will essentially concentrate on the influence of temperature gradients on the capillary effects and will not analyse in detail the influence of the variation of the saturation vapor partial pressure with temperature. This latter aspect is discussed in detail in [8], for situations where capillary effects dominate as well as for situations where gravity effects are significant. Interestingly, the pore network simulations presented in [8] indicate a significant influence of the saturation vapor partial pressure gradient (induced by the temperature gradient) on the drying process, especially in the latter stages of drying (not considered in the present paper that rather focus on the stages where the liquid phase is not yet completely broken up into liquid clusters of "finite" size). The influence of a surface tension gradient due to a thermal gradient is not considered, however, in the study by Huinink et al. [8].

On the experimental side, the theory of Philip and de Vries was confirmed by the comprehensive experimental study of Crausse [9]. The migration of moisture towards cold zones due to thermal gradients was clearly demonstrated. The data obtained by Crausse were used by Recan [10] in a numerical study. As reported in the review paper by Bories [11], the sensitivity study conducted by Recan also confirmed the significant influence of thermal gradients, at least for the material and the conditions studied by Crausse. In this respect, it is worth mentioning that the thermal gradients in Crausse's study were of the order of 1 °C/cm and that the porous material was a sand with most of the grains in the range 100–125 μm, i.e. a material of narrow pore size distribution (i.e. of weak disorder in the terminology of the network approach presented below). The results of Crausse and therefore the overall relevance of the Philip and de Vries model was further confirmed by the study of Rouger [12]. Here, it should be pointed out that the initial moisture contents of the porous samples were quite low in these experiments. In the present paper, we investigate the quite different situation where the sample is initially fully saturated and where viscous and gravity effects have a negligible influence. As discussed above,

this case leads to IP patterns and cannot be described adequately within the framework of continuum model owing to the occurrence of long range correlations in the phase distribution near the percolation threshold. In such a case, network approaches offer a much more suitable framework. Also, it should be emphasised that the general ability of continuum models to predict quantitatively the evaporation flux can be considered as poor. Hence the development of network models can be regarded as an effort to improve our understanding of the physics of drying, a (hopefully) necessary step towards more predictive models.

2. Pore network model

The pore network model developed for the present study is an extension of the model initially proposed by Prat [13]. As in most pore network studies of drying, a single component liquid is assumed (an exception is the work of Freitas and Prat [14] on the evaporation of a binary liquid). The gas phase is a binary mixture (vapor of the liquid + air, the vapor concentration being small compared to the air concentration). Throughout this paper, vapor will refer to the liquid vapor in the gas phase whereas the air/vapor mixture forming the gas phase will be simply termed the gas phase. As in most models of drying well below the boiling temperature, mass transfer in the gas phase is due to diffusion only. Assuming relatively large pores, the Kelvin effect is neglected. For simplicity, a perfectly wetting liquid is assumed. The pore space is conceptualized as a network of randomly sized pores (sites) joined by randomly sized throats (bonds). We used a square lattice as depicted in Fig. 2. Three edges of network are impervious (no mass transfer at these boundaries). The vapor escapes through the remaining open edge (top edge in Fig. 2). Initially, the network is completely saturated by the liquid. In the absence of thermal gradient, the drying algorithm for the IP domain reads [13]

(1) Every liquid cluster present in the network is identified.
(2) The bond connected to the already invaded region which has the lowest threshold capillary pressure is identified for each cluster.
(3) The evaporation flux at the boundary of each cluster is computed.
(4) For each cluster, the mass loss corresponding to the evaporation flux determined in step (3) is assigned to the bond identified in step (2).
(5) The bond (as well as the adjacent pore) eventually invaded is that which is the first to be completely drained among the bonds selected in step (2).
(6) The phase distribution within the network is updated.

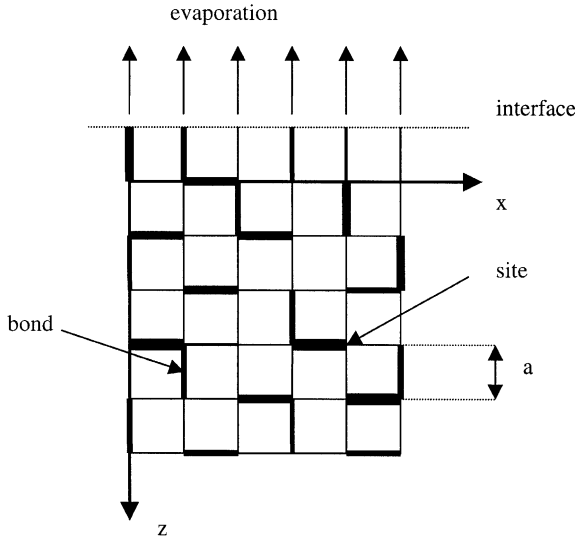

Fig. 2. 2D pore space square network of bonds (throats) and sites (pores).

The threshold capillary pressure of a bond (step (2)) is classically expressed as

$$P_{\mathrm{cth}} = \frac{2\gamma}{\ell} \tag{2}$$

where ℓ is the width of the considered bond.

At this stage, it is interesting to note that P_{cth} is a function of the surface tension γ and thereby of the temperature since γ varies with temperature. Hence, in the presence of thermal gradients, the temperature dependence of P_{cth} introduces a coupling between the heat transfer and the invasion process. A second modification induced by the presence of thermal gradients concerns the computation of the evaporation flux (step (3)) from the computation of the liquid vapor partial pressure in the gas phase. Under isothermal conditions, the equilibrium vapor partial pressure on the menisci is a constant (fixed by the imposed temperature). As the equilibrium vapor partial pressure is a function of temperature, the boundary condition on the menisci for the partial pressure field computation varies spatially in the presence of thermal gradients. This represents a coupling between the mass and heat transfers (since in turn the heat transfer depends on the evaporation flux). Thus, here, the transport by diffusion in the gas phase is expressed in terms of the vapor partial pressure. Assuming a quasi-steady transport, the equation to be solved over the gas phase reads,

$$\nabla\left(D\frac{P}{P-P_{\mathrm{v}}}\frac{M_{\mathrm{v}}}{RT}\nabla P_{\mathrm{v}}\right) = 0 \tag{3}$$

where D is the binary diffusion coefficient of the vapor in gas phase, P the gas phase total pressure, P_{v} the vapor

partial pressure, R the universal gas constant, M_v the vapor molecular weight and T the temperature. Eq. (3) is discretized over the gas phase domain by adapting a standard finite volume technique [15]. Assuming a one-dimensional transport in each bond, this leads to express the mass flux balance on each site ij of the network occupied by the gas phase as,

$$F_n + F_s + F_w + F_e = 0 \tag{4}$$

where subscripts n, s, w, e refer to the first neighbour top (north), bottom (south), left hand side (west) and right hand side (east) nodes of node ij. The discretized form of the flux reads:

$$F_i = D\ell_i e \frac{M_v}{RT}\frac{P_i - P_{ij}}{a} \quad \text{when neighbour site } i \text{ is a gas node}$$

$$F_i = D\ell_i e \frac{M_v}{RT}\frac{P_{sat} - P_{ij}}{(1-\beta)a/2} \quad \text{when neighbour site } i \text{ is a liquid node}$$

where e is the thickness of the network, P_{sat} the equilibrium vapor partial pressure, ℓ_i the width of the bond joining site ij to neighbour site i while $(1-\beta)a/2$ is the distance between site ij and the meniscus located at the entrance of the adjacent bond (when neighbour pore i is liquid). At the interfacial boundary (open edge of network), the vapor mass flux at the entrance of an interfacial bond is expressed as

$$F_e = h\ell e(P_v - P_{v\infty}) \tag{5}$$

where P_v is the vapor partial pressure at the considered interfacial site and $P_{v\infty}$ is the vapor partial pressure in the surrounding atmosphere. The mass transfer coefficient h is estimated assuming a diffusive layer of thickness δ at the interfacial boundary of the network, i.e. F_e is in fact computed as

$$F_e = D\frac{M_v}{RT}\ell e\frac{(P_v - P_{v\infty})}{\delta} \tag{6}$$

with $\delta = a/10$, i.e. the external diffusive transfer is 10 times as effective as the internal diffusive transfer over the lattice spacing a. This corresponds roughly to an external mass boundary layer of thickness $a/10$, i.e. 0.1 mm for the simulations discussed in Section 4. The system resulting from the discretization is solved by a conjugate gradient method. More details on the computation of the transport by diffusion on a network can be found in [14].

Naturally, an important new feature of the present model is the computation of the temperature field at each step of the invasion. Compared to the computation of the diffusive transport in gas phase the essential difference is that the thermal transport takes place not only within the pore space but also within the solid phase. As in previous pore network models including heat transfer [16,17] the energy equation is therefore discretized over a network twice finer than the pore space network, so that

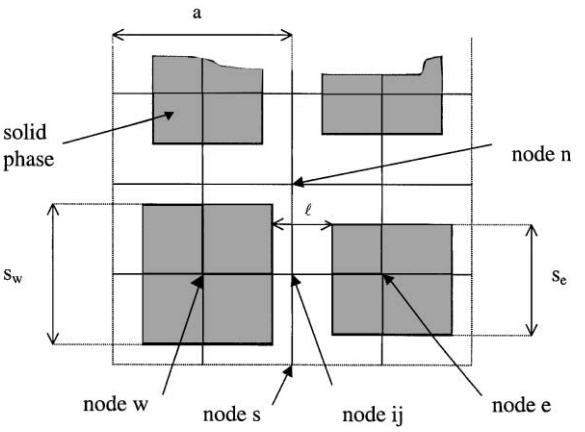

Fig. 3. Thermal network.

nodes of thermal network are located in the solid phase, as shown in Fig. 3. For the situations considered in the present paper (temperature well below the boiling temperature), heat transport by convection is negligible within the porous medium. Assuming a quasi-steady conductive heat transfer, the energy equation to be solved over the thermal network at each step of the invasion simply reads

$$\nabla(\lambda\nabla T) = 0 \tag{7}$$

where the thermal conductivity λ depends on the location within the network. As the solid phase is formed by isolated grains in the 2D pore space network model (see Fig. 2) some approximation should be made in order to model the solid phase as a connected one for the conductive heat transfer. In fact as shown in Fig. 3, there are five types of bond in the thermal network: (a) the bonds between two nodes located in the liquid phase, (b) the bonds between two nodes located in the gas phase, (c) the bonds joining a node in the gas phase to a node in the solid phase, (d) the bonds joining a node in the liquid phase to a node in the solid phase, (e) the bonds where a meniscus is located. For simplicity, the bonds corresponding to (a) and (d) are assigned λ_l^* as thermal conductivity and the bonds corresponding to (b) and (c) λ_v^*, where λ_l^* and λ_v^* are effective conductivities corresponding to the porous medium saturated by liquid and vapor respectively. It could be pointed out that the use of effective thermal conductivities is not consistent with the scale of description of the network model since effective conductivities are traditionally defined at Darcy's scale. In the context of our essentially qualitative study, using effective conductivities should be regarded here as a simple manner of introducing thermal connections within the solid phase. Using grain level conductivities, which was found to be a satisfactory procedure in a previous work [17] is in fact conventional in such models (e.g.

[16]) and is therefore used here again. λ_l^* and λ_v^* are estimated according to a parallel arrangement model,

$$\lambda_i^* = \varepsilon\lambda_i + (1-\varepsilon)\lambda_s \quad i = l, v \tag{8}$$

where ε is the porosity, λ_v, λ_l, λ_s are the thermal conductivities of the vapor, liquid and solid phases respectively. Again, we only need reasonable estimates of the thermal conductivity of the thermal network bonds. Any other reasonable approximations of the thermal conductivities could have been used as well. Adapting finite volume discretization concepts leads to express the heat flux balance on each site ij of the thermal network as,

$$\phi_n + \phi_s + \phi_w + \phi_e = S_{ij} \tag{9}$$

with $S_{ij} = 0$ for nodes that are not neighbour of a meniscus. When there is no meniscus located between two nodes, the discretized flux between the two nodes is expressed as

$$\phi_i = \lambda^* \frac{(T_{ij} - T_i)}{a/2} s_i \quad i = n, s, w, e \tag{10}$$

where $\lambda^* = \lambda_l^*$ or λ_v^* depending on the fluid occupying the involved bond of the pore space network, s_i is the exchange surface between the two nodes (see Fig. 3). Subscripts n, s, w, e refer here to the first neighbour top (north), bottom (south), left hand side (west) and right hand side (east) nodes of node ij on the thermal network.

When a meniscus is present between two nodes, the discretization is a little bit more involved. Consider for instance the case depicted in Fig. 4. On the meniscus, the heat flux balance reads

$$\left[\lambda_v^* \left.\frac{\partial T}{\partial x}\right|_v - \lambda_l^* \left.\frac{\partial T}{\partial x}\right|_l\right] \ell e = \Delta h_{vap} F \tag{11}$$

where Δh_{vap} is the enthalpy of vaporization per unit mass, F is the evaporation mass flux at the meniscus. The discretized form of Eq. (11) is written as

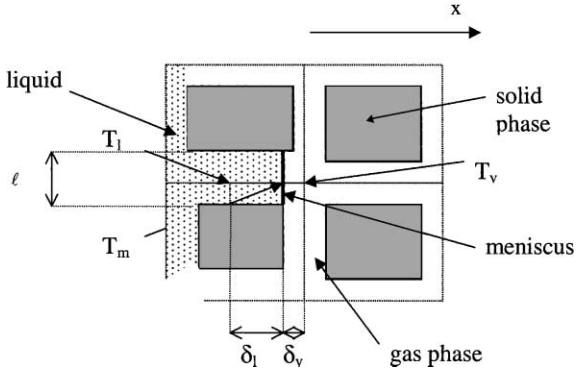

Fig. 4. Thermal network, example of bond containing a meniscus.

$$\left[\lambda_v^* \frac{(T_v - T_m)}{(1-\beta)a/2} - \lambda_l^* \frac{(T_m - T_l)}{\beta a/2}\right] \ell e = \Delta h_{vap} F \tag{12}$$

where T_m is the temperature at the meniscus. From the above equation, one can express T_m as a function of T_l, T_v and F. This leads to the following expressions for ϕ_e (node "l"), ϕ_w (node "v"), S_{le} (contribution to source term S in the heat flux balance equation for node "l") and S_{vw} (contribution to source term S in the heat flux balance equation for node "v")

$$\phi_e = \frac{\lambda_l^* \ell e}{\delta_l}\left(1 - \left(\frac{\lambda_v^*}{\delta_v} + \frac{\lambda_l^*}{\delta_l}\right)^{-1} \frac{\lambda_l^*}{\delta_l}\right) T_l - \frac{\lambda_l^* \ell e}{\delta_l} \times \left(\left(\frac{\lambda_v^*}{\delta_v} + \frac{\lambda_l^*}{\delta_l}\right)^{-1} \frac{\lambda_v^*}{\delta_v}\right) T_v \tag{13}$$

$$\phi_w = \frac{\lambda_v^* \ell e}{\delta_v}\left(1 - \left(\frac{\lambda_v^*}{\delta_v} + \frac{\lambda_l^*}{\delta_l}\right)^{-1} \frac{\lambda_v^*}{\delta_v}\right) T_v \times -\frac{\lambda_v^* \ell e}{\delta_v}\left(\left(\frac{\lambda_v^*}{\delta_v} + \frac{\lambda_l^*}{\delta_l}\right)^{-1} \frac{\lambda_l^*}{\delta_l}\right) T_l \tag{14}$$

$$S_{le} = -\frac{\lambda_l^* \ell e}{\delta_l}\left(\frac{\lambda_v^*}{\delta_v} + \frac{\lambda_l^*}{\delta_l}\right)^{-1} \frac{\Delta h_{vap} F}{\ell e} \tag{15}$$

$$S_{vw} = -\frac{\lambda_v^* \ell e}{\delta_v}\left(\frac{\lambda_v^*}{\delta_v} + \frac{\lambda_l^*}{\delta_l}\right)^{-1} \frac{\Delta h_{vap} F}{\ell e} \tag{16}$$

where $\delta_v = (1-\beta)a/2$ and $\delta_l = \beta a/2$.

Regarding the conditions at the boundaries of the thermal network, zero flux conditions are imposed on the lateral edges whereas the temperature is imposed on the top and bottom edges ($T = T_t$ and $T = T_b$ respectively). This is of course only an approximation of the heat transfer problem at the top boundary, which is, however, consistent with the fact that the evaporation fluxes are small in our simulations. The system resulting from the discretization is solved by a conjugate gradient method.

Taking into account the thermal gradients finally leads to the following algorithm:

(1) Every liquid cluster present in the network is identified.
(2) The evaporation flux at the boundary of each cluster is computed.
(3) The temperature field is computed.
(4) The bond connected to the already invaded region which has the lowest threshold capillary pressure is identified for each cluster.
(5) For each cluster, the mass loss corresponding to the evaporation flux determined in step (2) is assigned to the bond identified in step (4).
(6) The bond (as well as the adjacent pore) eventually invaded is that which is the first to be completely drained among the bonds selected in step (4).

(7) The phase distribution within the network is updated and the procedure is repeated until a specified number of bonds has been invaded.

Owing to the heat and mass transfer coupling, an iteration procedure should be used for steps (2) and (3). However for the situations considered in the present paper, the change in the temperature field is small between two invasions. Therefore the iteration procedure need not to be enforced and it is sufficient to use the temperature of the preceding stage for computing the evaporation flux of step (2).

3. Theoretical aspects

Before discussing the simulations, it is interesting to explore the influence of thermal gradients on the invasion from a theoretical standpoint. As discussed in Section 1 the capillary pressure is constant spatially in the absence of significant gravity and viscous forces (IP domain). Thus, for a perfectly wetting liquid,

$$P_c = \frac{2\gamma}{r} = \text{constant} \tag{17}$$

where r is the local radius of curvature of the menisci ($r \approx \ell/2$). In the presence of thermal gradient, Eq. (17) implies that the radius of curvature of the menisci varies spatially since the surface tension γ depends on temperature. Assuming for simplicity, a uniform bond width distribution in the range $[\ell_{\min}, \ell_{\max}]$, we can express the fraction p of accessible bonds corresponding to P_c as

$$p = \frac{\ell_{\max} - 2r}{\Sigma} \tag{18}$$

where $\Sigma = \ell_{\max} - \ell_{\min}$.

As γ varies spatially in the problem under study, we deduce from the above equations,

$$\frac{dp}{dz} \propto -\frac{1}{\Sigma}\frac{d\gamma}{dT}\frac{dT}{dz} \tag{19}$$

where z is the spatial coordinate directed from the open edge towards the bottom edge of the network. Hence, in this problem, the tension surface gradients induced by the thermal gradient impart a gradient in p. As discussed in Section 1, we can distinguish two different global patterns, depending on whether invasion is in a stabilizing gradient (i.e. $dp/dz < 0$, that is with the chosen system of coordinates $(d\gamma/dT)(dT/dz) > 0$), or a destabilizing gradient ($dp/dz > 0$, that is $(d\gamma/dT)(dT/dz) < 0$). For water (as well as for the other liquids), the surface tension decreases with increasing temperature, i.e. $d\gamma/dT < 0$. Therefore, we expect an IP process in a destabilizing gradient when $dT/dz > 0$ and stabilizing gradient patterns when $dT/dz < 0$.

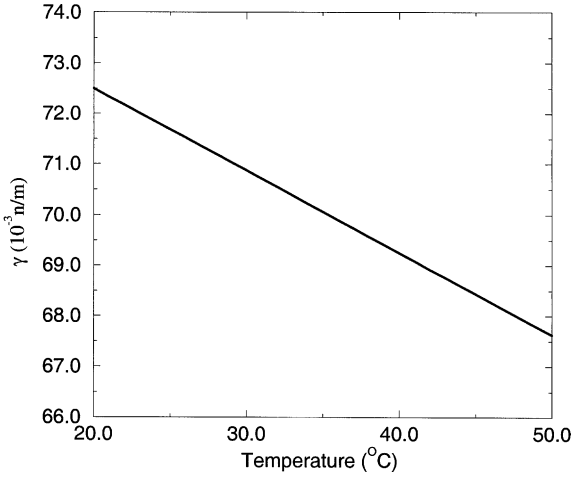

Fig. 5. Water surface tension as a function of temperature.

3.1. Influence of disorder

Eq. (19) indicates that the probability gradient depends not only on the surface tension gradient but also on the disorder Σ. More precisely, Eq. (19) shows that the effect of surface tension gradient will be significant only if the disorder is not too large. Thus, for porous materials characterized by broad pore size distribution, the effect of surface tension gradients can be expected to become negligible, and IP patterns are expected (we recall that the influence of gravity or viscous effects is ignored in this analysis).

3.2. Order of magnitude estimates

Consider the case of porous medium saturated by water with temperatures in the range 20–50 °C. As can be deduced from Fig. 5 showing the evolution of surface tension as a function of temperature, $d\gamma/dT \approx -0.17 \times 10^{-3}$ N/m/°C. Previous simulations for fronts stabilized by gravity ([5]) indicate that dp/dz^* (where $z^* = z/a$) must be of the order of 10^{-3} for observing significant gradient effects on networks of similar size as those used for the simulations presented hereafter. According to Eq. (19), this leads to temperature gradient dT/dz^* of the order of 0.2 °C/lattice unit (assuming the same disorder as in the above-mentioned simulations), that is of the order of 1 °C/cm for a lattice spacing of 10^{-3} m.

4. Simulations

Evaporation of pure water into air is considered in the simulations, so that the values of all physical properties (D, M_v, γ, etc.) relative to the fluids are those corresponding to the air–water system.

4.1. High thermal conductivity limit

When the thermal conductivity of the solid phase is high, the porosity not too high and the solid phase well connected, then the effective thermal conductivity of the regions saturated by liquid and that of the regions invaded by the gas phase become comparable. In this limit, for simplicity, we can reasonably assume that the effective thermal conductivity is independent of the saturation. Moreover, if we neglect the heat transfer associated with the phase change (this assumption will be discussed further in Section 4.2), the solution of the thermal problem becomes trivial ($T = ((T_b - T_t)/L)z + T_t$). In this limit, we do not need to solve the thermal problem numerically and can therefore perform simulations on much larger networks than those that can be reasonably considered when comptutations of the temperature field must be carried out (we recall that the thermal lattice contains twice as much computation nodes compared to the pore space lattice). Therefore, this limit enables one to gain insight into the influence of the thermal gradient and disorder for a much less computational effort than for full simulations. The simulations discussed in this section are summarized in Table 1 and have been performed over a 150×150 pore network (with a lattice spacing $a = 1$ mm). The average bond size was 0.30 mm. The phase distributions obtained for a weak disorder ($\Sigma^* = 0.03$) are shown in Fig. 6. In accordance with the theoretical prediction the phase distributions obtained for $dT/dz > 0$ are characteristic of IP in a destabilizing gradient (IPDG) patterns. IPDG patterns in drying are discussed in [6]. There are three main steps in the invasion: the single branch growth (left hand side top image in Fig. 6), the invasion front step, the disconnected cluster erosion step. The left hand side bottom image in Fig. 6 corresponds to the end of step (2). Patterns for $dT/dz < 0$ (right hand side images in Fig. 6) are characteristic of IPSG in drying, i.e. a traveling stabilized two phase region between a fully saturated region and a dry region.

As can be seen from Fig. 7, the marked differences between invasion in a positive thermal gradient and a negative thermal gradient discussed above completely disappear for a sufficiently large disorder (in agreement with the theoretical predictions). In fact, drying IP patterns are recovered in this case.

Table 1
Simulations performed in the high conductivity limit

	T_t (°C)	T_b (°C)	dT/dz (°C/cm)	Σ^*
S1	20	35	+1	0.03
S2	35	20	−1	0.03
S3	20	35	+1	0.5
S4	35	20	−1	0.5

Fig. 8 shows the evolution of the overall saturation as a function of time for the various cases considered in this section. When the disorder is low enough for the sign of the thermal gradient to influence the invasion (curves corresponding to $\Sigma^* = 0.03$ in Fig. 8), the drying kinetics are greatly affected. As can be seen from Fig. 8, drying is much faster when an IPDG pattern develops (i.e. $dT/dz > 0$). This is kind of paradoxical if one considers that the open edge of network is 15 °C colder for the case $dT/dz > 0$ compared to the case $dT/dz < 0$ but in fact consistent with the phase distributions depicted in Fig. 6 since the dry-out of the open edge region of network occurs much later for $dT/dz > 0$. Hence, this indicates that blowing a colder air than the initial temperature sample can lead to a much faster drying than blowing a warmer air when the disorder of the sample is low enough for IPDG pattern to develop. As illustrated in Fig. 8, this is the opposite which is true when the disorder is sufficient for the invasion pattern to be not affected by the presence of thermal gradient. These results are the consequence of the interplay between the external mass transfer (see Eqs. (5) and (6)) and the evolution of the liquid phase distribution at the network interface. As explained in the comments below Eq. (6) and in accordance with the general features of convective drying, the external mass transfer is significantly more effective than the diffusive transport in gas phase within the network. As a result, maintaining wet the surface of the network in the case $dT/dz > 0$ overcompensates here the fact that the saturation vapor partial pressure is significantly lower for a colder temperature. This can be simply illustrated assuming that the evaporation front is located at a distance δ_i from the interface within the material. Then, according to Eq. (6) and assuming for simplicity $P_{v\infty} = 0$, the evaporation flux scales as,

$$F_e \propto \frac{P_{vs}}{(\delta + \delta_i)} \tag{20}$$

Considering two different temperatures T_1 and T_2 with $T_1 < T_2$, one deduces from Eq. (20) that

$$\frac{F_e(T_1)}{F_e(T_2)} \propto \frac{(\delta + \delta_i(T_2))}{(\delta + \delta_i(T_1))} \frac{P_{vs}(T_1)}{P_{vs}(T_2)} \tag{21}$$

Assuming now that $\delta_i(T_1) = 0$ (the interface is wet for the coldest temperature), it is obtained

$$\frac{F_e(T_1)}{F_e(T_2)} \propto \frac{(\delta + \delta_i(T_2))}{\delta} \frac{P_{vs}(T_1)}{P_{vs}(T_2)} \tag{22}$$

which shows that

$$\frac{F_e(T_1)}{F_e(T_2)} > 1 \quad \text{when} \quad \frac{(\delta + \delta_i(T_2))}{\delta} \frac{P_{vs}(T_1)}{P_{vs}(T_2)} > 1 \tag{23}$$

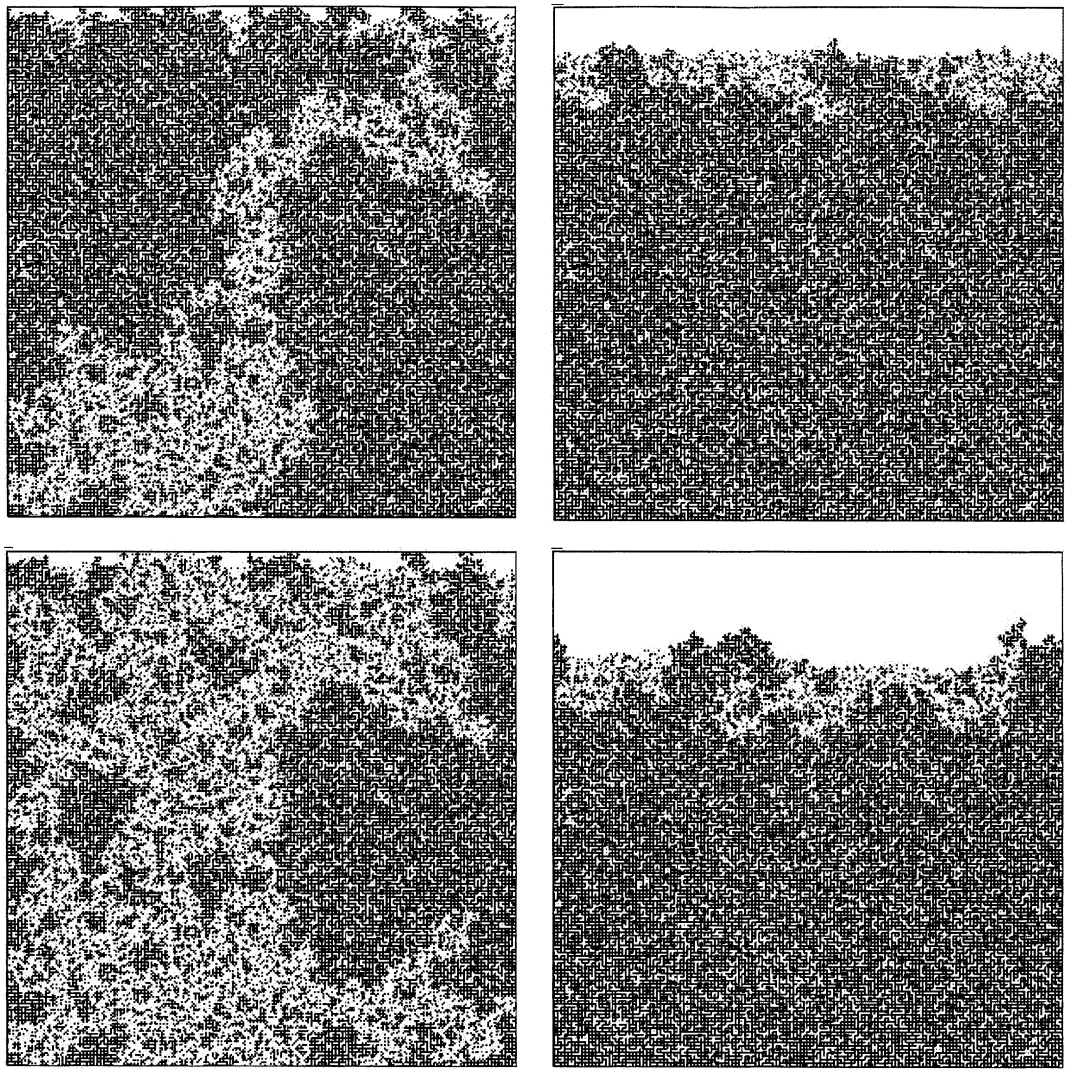

Fig. 6. Phase distribution for 5000 and 10 000 invaded bonds for a weak disorder ($\Sigma^* = 0.03$). Liquid phase in black, gas phase in white. Vapor escapes through top edge of network. Images on the left hand side column are for $dT/dz = 1$ °C/cm. Right hand side images are for $dT/dZ = -1$ °C/cm.

Eq. (23) can be still simplified assuming the external transfer resistance is small compared to the internal one, i.e. $\delta \ll \delta_i$. This finally leads to

$$\frac{F_e(T_1)}{F_e(T_2)} > 1 \quad \text{when} \quad \frac{\delta_i(T_2)}{\delta}\frac{P_{vs}(T_1)}{P_{vs}(T_2)} > 1 \tag{24}$$

which clearly indicates that a colder interface temperature can lead to higher evaporation rates provided that (i) the surface remains wet when cold (i.e. $\delta_i(T_1) = 0$ for a IPDG pattern) and (ii) the internal transfer resistance (associated with the development of a IPSG pattern) is sufficiently greater than the external transfer resistance (i.e. $\delta_i(T_2) > \delta P_{vs}(T_2)/P_{vs}(T_1)$).

4.2. Influence of thermal conductivity contrast

In contrast with the preceding section, we explore in this section situations in which the apparent thermal conductivity of the regions saturated by the gas phase is significantly lower than the apparent thermal conductivity of the regions saturated by the liquid. The thermal conductivity contrast (between the gas saturated and liquid saturated regions) can be more or less important depending on the porosity, the connectivity of solid matrix and the thermal conductivity of the solid phase. Our aim being to gain some insight into the influence of the thermal conductivity contrast, we consider simply

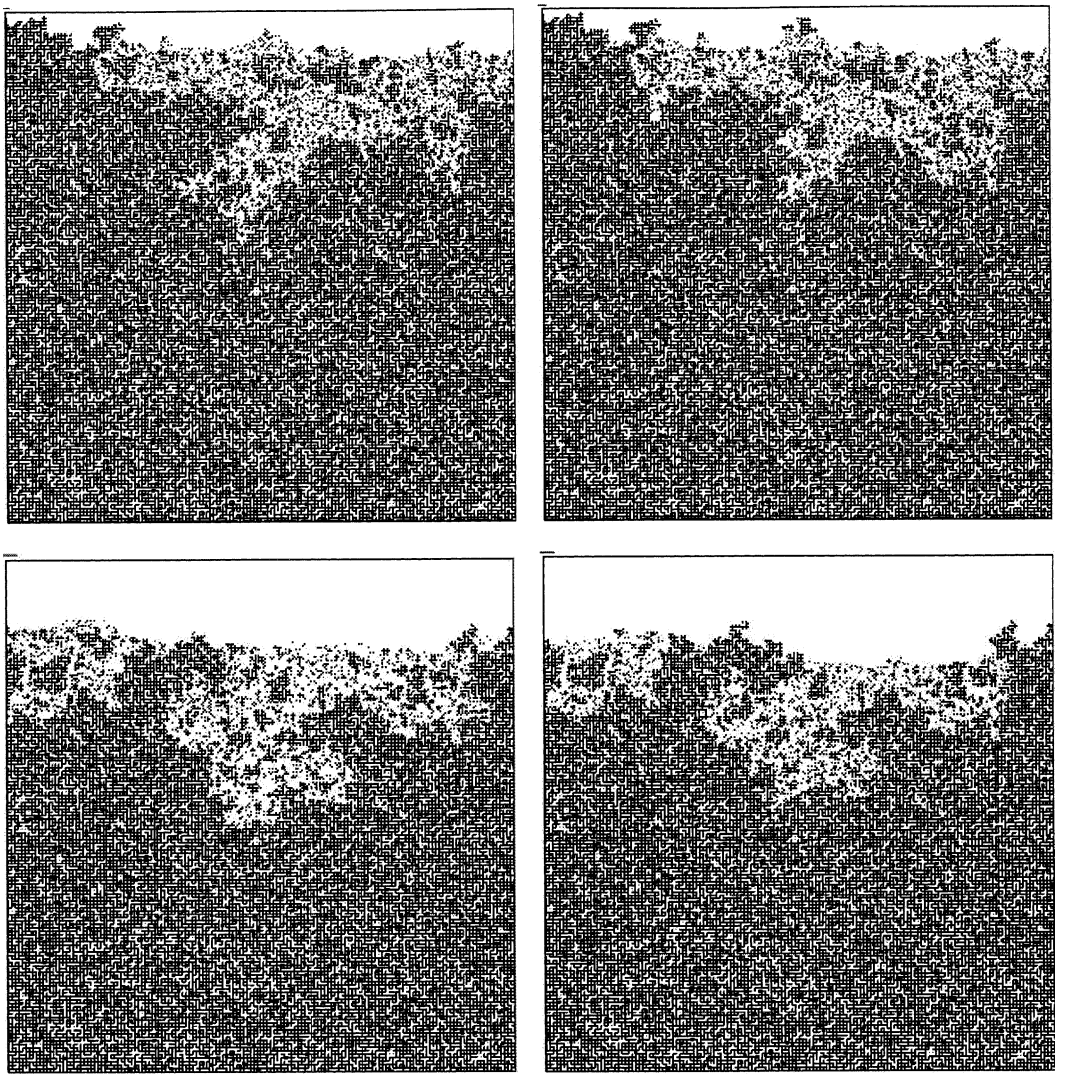

Fig. 7. Phase distribution for 5000 and 10 000 invaded bonds for a greater disorder ($\Sigma^* = 0.5$). Liquid phase in black, gas phase in white. Vapor escapes through top edge of network. Images on the left hand side column are for $dT/dz = 1$ °C/cm. Right hand side images are for $dT/dz = -1$ °C/cm.

the case where λ_v^* is 10 times as small as λ_l^*. More specifically, we adopted the values $\lambda_v^* = 0.2$ W/m/°C and $\lambda_l^* = 2$ W/m/°C. These values correspond to the sand used by Crausse [9,18] in his experiments. In order to reduce the computational time, we consider a smaller network (100×100) but impose a weaker disorder ($\Sigma^* = 0.005$) than in Section 4.1 (see Section 5 for a discussion about the factors controlling the occurrence of IPG patterns in the presence of thermal gradients). As before, we compare the results obtained for positive thermal gradients and negative thermal gradients. More precisely, the simulations were performed for the conditions summarised in Table 2. As can be seen from Table 2, full simulations (i.e. including the computation of temperature field at each step of invasion) were also performed for high thermal conductivities in the absence of contrast. The results obtained for this case are fully consistent with the results discussed in Section 4.1. In particular, the temperature fields are only marginally affected by the change of phase. As a result, these fields are very close to those considered in Section 4.1. As an example, this is illustrated in Fig. 9 which shows the temperature field obtained for simulation S5 when 5000 bonds have been invaded. The phase distributions for simulations S5 (resp. S6) are not significantly different from those obtained for simulation S7 (resp. S8). The phase distributions corresponding to S7 and S8 are shown in Fig. 10. As predicted, IPDG patterns are ob-

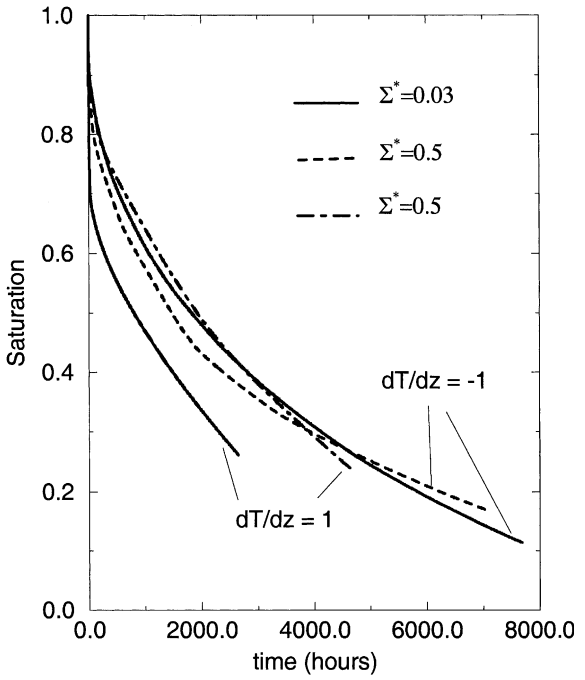

Fig. 8. Evolution of overall saturation as a function of time (thermal gradients are expressed in °C/cm).

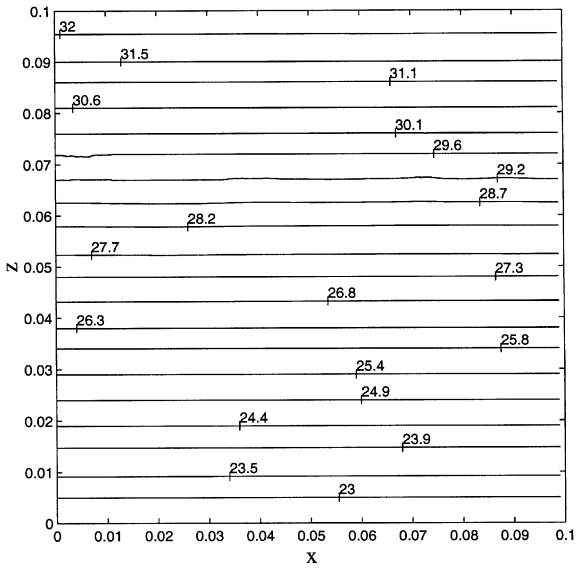

Fig. 9. Example of temperature field computed for a low thermal conductivity contrast (simulation S5 for 5000 invaded bonds). Contrary to remaining of paper z is oriented from bottom to top (open edge) in the figure.

tained for a positive thermal gradients and IPSG patterns for negative ones. Naturally, when the thermal conductivity contrast is marked, the temperature field differs from the simple conduction field in an homogeneous medium. This is illustrated in Fig. 11 which shows examples of temperature fields corresponding to simulations S7 and S8. Interestingly, one observes that the thermal gradient is non-constant along z contrary to the situations discussed previously. For positive gradients (IPDG pattern), the thermal gradients are greater than the average gradient in the invaded region. This may favor the development of an IPDG pattern (i.e. lead for example to a maximum size of trapped clusters lower than for a weaker thermal conductivity contrast). On the contrary, for negative gradients (IPSG pattern) the thermal gradients tend to be lower than the average gradient in the invasion region. This may limit the development of an IPSG pattern (i.e. lead for example to a greater average extension of the front) compared to cases where the thermal conductivity contrast is lower. Our simulations indicate, however, that this effect remains marginal for thermal conductivity contrast up to 10 (the slight differences observed between the phase distributions of simulations S5, S6 (not shown in this paper) and S7, S8 are, however, consistent with the above discussion).

5. Discussions

It could be pointed out that the values of the disorder parameter Σ associated with significant effects of thermal gradient orientation for the simulations presented in Section 4 are quite small. The value $\Sigma^* = 0.03$ (Section 4.1) corresponds to a relative variation of only 10% in the pore size whereas the value 0.005 (Section 4.2) corresponds to a relative variation still smaller (≈2%!). However, it may be observed that porous materials with

Table 2
Simulations performed with full computation of thermal field

	T_t (°C)	T_b (°C)	dT/dz (°C/cm)	λ_v^* (W/m/°C)	λ_l^* (W/m/°C)	Σ^*
S5	22.5	32.5	+1	50	50	0.003
S6	32.5	22.5	−1	50	50	0.003
S7	22.5	32.5	+1	0.2	2.0	0.003
S8	32.5	22.5	−1	0.2	2.0	0.003

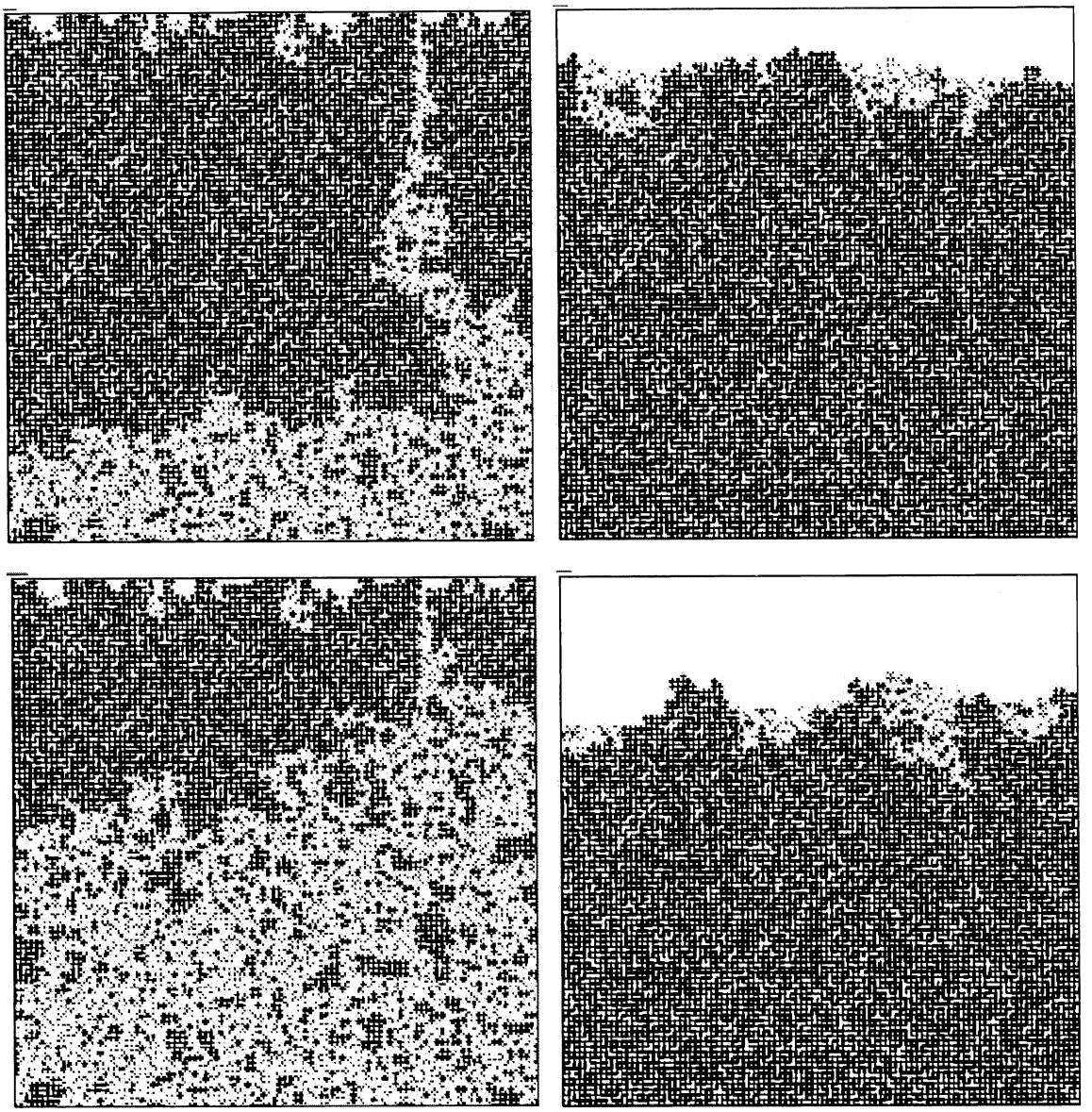

Fig. 10. Phase distribution for 2500 and 5000 invaded bonds (simulations S7 and S8). Liquid phase in black, gas phase in white. Vapor escapes through top edge of network. Images on the left hand side column are for $dT/dz = 1$ °C/cm. Right hand side images are for $dT/dz = -1$ °C/cm.

very narrow pore size distribution are not uncommon. As mentioned in the introduction, the relative variation in grain size for the sand used by Crausse [9] is of the order of 25%. For the chalk used in te experiments reported in [19], most pore sizes are in the range 0.1–0.6 μm whereas the mercury invasion was found to be controlled essentially by one pore size for the rocks studied by Tournier [20]. Other examples of materials with narrow pore size distribution are also reported in the book of Dullien [21]. Nevertheless, the disorder in our simulations may still sound unrealistically small. It could be argued that Σ reflects the disorder in the throat size and not the disorder in the pore size but it is more important to recognize that Σ is not the sole parameter controlling the occurrence of IPDG or IPSG patterns. From previous works (see [5] and references therein) it is known that the characteristic scale L_T of a front (approximately liquid–vapor region of limited extension) associated with gradient percolation effects can be expressed as power-law of the occupation probability

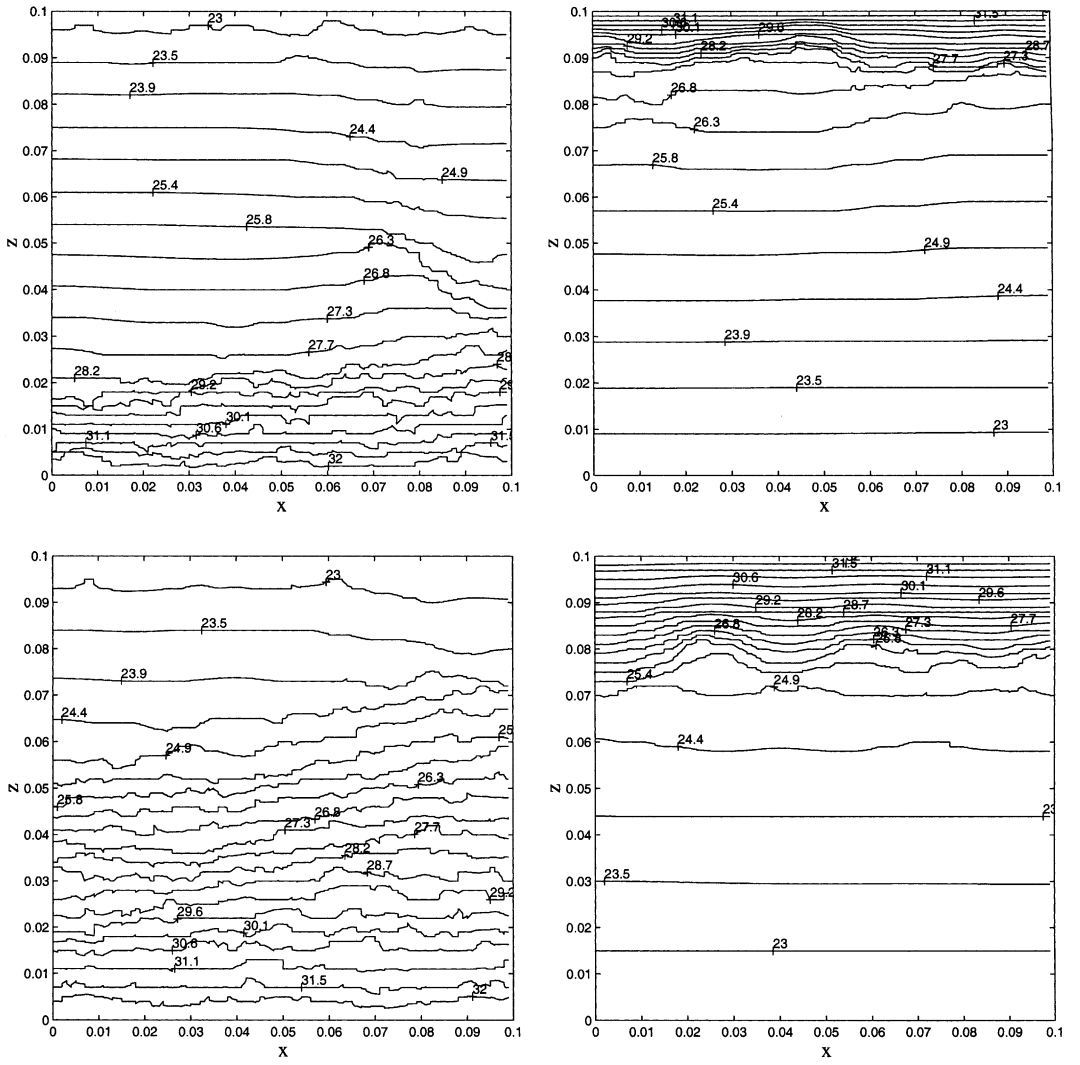

Fig. 11. Temperature fields corresponding to the phase distributions depicted in Fig. 10 Contrary to remaining of paper z is oriented from bottom to top (open edge) in the figure.

gradient, that is in the present context (taking into account Eq. (19)),

$$\frac{L_T}{a} \propto \left(\frac{\gamma^{-1}}{(\Sigma/a)} \left| \frac{d\gamma}{dT} \right| \left| \frac{dT}{dz^*} \right| \right)^{-\alpha} \tag{25}$$

where $z^* = z/a$ and α is a positive universal exponent that only depends on the dimensionality of the lattice ($\alpha = 0.52$ in two dimensions as shown in [5]).

For a given porous medium sample of size L, one therefore expects IP pattern when $L_T > L$ and IPG patterns induced by thermal gradients when $L_T < L$ (we recall we assume here $L_g > L$ and $L_{cap} > L$ so that gradient percolation effects induced by gravity or viscosity effects are not considered in the discussion). Hence, IPG patterns will be observed when

$$m\left(\frac{\gamma^{-1}}{(\Sigma/a)} \left| \frac{d\gamma}{dT} \right| \left| \frac{dT}{dz^*} \right| \right)^{-\alpha} < \frac{L}{a} \tag{26}$$

where m is a numerical prefactor that solely depends on the porous medium microstructure. The various patterns that can be expected are summarized in Fig. 12. Again, the diagram shown in Fig. 12 is pertinent as long as L_g and L_{cap} are larger than L_T. Consistently with Eq. (26), IPG patterns with the 100×100 network of Section 4.2 were obtained for a smaller disorder than the one imposed for the simulations over the 150×150 networks of Section 4.1 (the lattice spacing being the same and the thermal gradients being of the same order of magnitude). More interestingly, Eq. (26) indicates that IPG patterns due to thermal gradients could be observed for

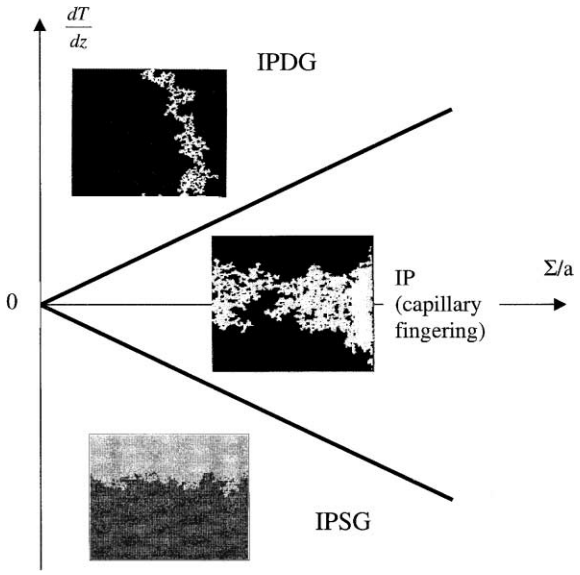

Fig. 12. Drying phase diagram in the presence of thermal gradients and in the absence of significant gravity or viscosity effects.

networks of significantly larger disorders than those considered in Section 4 provided that the thermal gradient and/or the sample size L are sufficiently large.

6. Conclusions

The primary objective of this paper was to present a pore network model of drying in the presence of thermal gradients.

A second objective of the present paper was to illustrate through pore network simulations the effect of the surface tension gradients induced by thermal gradients on the phase distribution during drying. The numerical results are consistent with the expected influence of the surface tension gradients associated with the spatial variation of temperature. In agreement with the theory of IP in a gradient, IPSG or IPDG patterns can be expected depending on the sign of the thermal gradient. As increasing the porous medium disorder has an effect that is equivalent to an increase in capillarity, IPSG and IPDG patterns are expected for sufficiently weakly disordered porous medium. This has been also illustrated through the simulations. Finally, a qualitative drying phase diagram has been proposed for delineating the various patterns that are expected as a function of thermal gradient and disorder parameter. This diagram is pertinent to situations where occupation probability gradients induced by viscous or gravity effects are negligible. On the basis of the present work on the effect of thermal gradients and previous works on the influence of viscous or gravity effects (e.g. [5] and references therein), it would not be difficult, however, to delineate the various patterns that can be expected according to the relative influence of disorder, thermal gradients, viscous, gravity and capillary effects.

The results presented also indicate the possibility of a somewhat paradoxical convective drying situation when thermal gradients and disorder are such that IPG patterns develop. In this case contrary to more conventional situations, it may be much more efficient to blow an air colder than the porous medium initial temperature.

In this paper, only 2D networks were considered. It is well known that there exist significant differences between IP in 2D and 3D systems. In this respect, it would be interesting to develop a 3D version of the present pore network model, especially for studying the influence of thermal gradients on drying rates. However, this does not invalidate the relevance of the main qualitative results of the present paper to 3D systems. Therefore, the phase diagram of Fig. 12 applies also to 3D systems (for first insights into drying in 3D within the frameworks of the network approach and IP theory (see [22,23]).

The present version of the pore network model can certainly be improved. Regarding the study of drying rates, it would be interesting to take into account the liquid film flows in the model since it has been shown that they can affect the drying rates [24]. In the presence of thermal gradients, local liquid condensation can occur within the pore space, (e.g. [25] and references therein). This effect is partly included in the presence version of the model but without simulating local re-imbibition (it is implicitly assumed that the re-imbibition phenomena are negligible for the drying conditions considered in the present study). Modelling imbibition on pore networks during drying remains a challenge that would deserve future works (see however [8]). It can reasonably be surmised that film flow and local imbibition effects influence only marginally the occurrence of various patterns discussed in the present work. Nevertheless, it would be certainly interesting to perform experiments aiming at validating the findings of the present paper as well as the results discussed in [8]. Work in this direction is in progress.

References

[1] O.A. Plumb, in: K. Vafai (Ed.), Transport Phenomena in Porous Media: Modeling the Drying Process, Handbook of Porous Media, Marcel Dekker, 2000, pp. 755–785, Chapter 17.

[2] M. Prat, Recent advances in pore-scale models for drying of porous media, Chem. Eng. J. 86 (1–2) (2002) 153–164.

[3] Y.C. Yortsos, A.K. Stubos, Phase change in porous media, Curr. Op. Coll. Interf. Sci. 6 (2001) 208–216.
[4] A.G. Yiotis, A.K. Stubos, A.G. Boudouvis, Y.C. Yortsos, A 2-D pore-network model of the drying of single-component liquids in porous media, Adv. Wat. Res. 24 (2001) 439–460.
[5] M. Prat, F. Bouleux, Drying of capillary porous media with stabilized front in two-dimensions, Phys. Rev. E 60 (1999) 5647–5656.
[6] J.B. Laurindo, M. Prat, Numerical and experimental network study of evaporation in capillary porous media. Phase distributions, Chem. Eng. Sci. 51 (23) (1996) 5171–5185.
[7] J.R. Philips, D.A. deVries, Moisture movement in porous materials under temperature gradient, Trans. Am. Geophys. Union 38 (1957) 222–232.
[8] H.P. Huinink, L. Pel, M.A.J. Michels, M. Prat, Drying processes in the presence of temperature gradients-pore-scale modelling, Eur. Phys. J. B., submitted for publication.
[9] P. Crausse, Etude fondamentale des transferts couplés de chaleur et d'humidité en milieu poreux non-saturé, Thèse Doctorates-Sciences, INP Toulouse, France, 1983.
[10] M. Recan, Simulation numérique du comportement thermique et hydrique d'un sol nu. Application à l'étude de l'évaporation par télédétection, Thèse de Docteur–Ingénieur de l'INP Toulouse, France, 1982.
[11] S. Bories, Fundamentals of drying capillary-porous bodies, in: S. Kakac, B. Kilkis, F. Kulacki, F. Arinc (Eds.), Convective Heat and Mass Transfer in Porous Media, NATO ASI Series E, vol. 196, Kluwer, Dordrecht, 1991, pp. 391–434.
[12] P. Rouger, Séchage des poreux granulaires par thermomigration: analyse théorique et résultats expérimentaux, Thèse INP Grenoble, France, 1988.
[13] M. Prat, Percolation model of drying under isothermal conditions in porous media, Int. J. Multi. Flow 19 (1993) 691–704.
[14] D.S. Freitas, M. Prat, Pore network simulation of evaporation of a binary liquid from a capillary porous medium, Transp. Porous Media 40 (2000) 1–25.
[15] S.V. Patankar, Numerical Heat Transfer and Fluid Flow, Hemisphere Publishing Corporation, 1980.
[16] C. Satik, Y.C. Yortsos, A pore network study of bubble growth in porous media driven by heat transfer, J. Heat Trans.—T. ASME 118 (1996) 455–462.
[17] C. Figus, Y. Le Bray, S. Bories, M. Prat, Heat and mass transfer with phase change in a porous structure partially heated. Continuum model and pore network simulations, Int. J. Heat Mass Trans. 42 (1999) 2257–2569.
[18] P. Crausse, G. Bacon, S. Bories, Etude fondamentale des transferts couplés de chaleur et de masse en milieu poreux, Int. J. Heat Mass Trans. 24 (1981) 991–1004.
[19] D.D. Morel, B. Bourbiaux, M. Latil, B. Thiebot, Diffusion effects in gas flooded light oil fractured reservoirs, SPE paper 20516 (1990) 433–446.
[20] B. Tournier, Transferts par capillarité et évaporation dans des roches—rôle des structures de porosité, Thèse Université Strasbourg I—Louis Pasteur, France, 2001.
[21] F.A.L. Dullien, Porous Media. Fluid Transport and Pore Structure, Academic Press, 1992.
[22] Y. Le Bray, M. Prat, Three-dimensional pore network simulation of drying in capillary porous media, Int. J. Heat Mass Trans. 42 (1999) 4207–4224.
[23] I.N. Tsimpanogiannis, Y.C. Yortsos, S. Poulou, N. Kanellopoulos, A.K. Stubos, Scaling theory of drying in porous media, Phys. Rev. E 59 (4) (1999) 4353–4365.
[24] J.B. Laurindo, M. Prat, Numerical and experimental network study of evaporation in capillary porous media. Drying rates, Chem. Eng. Sci. 53 (12) (1998) 2257–2269.
[25] L. Gu, C.K. Ho, O.A. Plumb, S.W. Webb, Diffusion with condensation and evaporation in porous media, in: Proceedings of 7th AIAA/ASME Joint Thermophysics and Heat Transfer Conference, Alburquerque, NM, 1998.